**

High-Speed Mid-Wave Infrared Uni-Traveling Carrier Photodetector with Inductive Peaked Dewar Packaging

Zhijian Shen, Jinshan Yao, Jian Huang, Zhecheng Dai, Luyu Wang, Fengyu Liu, Xinbo Zou, Bo Peng, Weimin Liu, Hong Lu, and Baile Chen

Abstract— Recently, there has been a growing demand for high-speed mid-wave infrared (MWIR) photodetectors (PDs) driven by the emergence of new fields, such as free-space communication and frequency comb spectroscopy. In this study, we investigated a high-speed InAs/GaSb type-II superlattice (T2SL) MWIR uni-traveling carrier (UTC) PD with relatively low dark current and high responsivity. We also perform an inductive peaked dewar packaging on the PD to be user-friendly and allow cryogenic operation. The original on-wafer PD shows a dark current density of 54.05 A/cm^2 and a 4.5 μm of no less than 0.36 A/W, with a 3-dB bandwidth of 3.83 GHz. The inductive-peaked device in dewar packaging demonstrates a dark current density of 1.65×10^{-5} A/cm^2 and a 4 μm responsivity of 0.39 A/W at 77 K, with a 3-dB bandwidth of 5.29 GHz.

Keywords—Mid-wave infrared high-speed photodetector, uni-traveling carrier photodiode, InAs/GaSb type-II superlattice, dewar packaging, inductive peaking, bonding wires

I. INTRODUCTION

MWIR PDs find extensive application in various fields, such as chemical detection, security and defense, astronomy, and medical diagnostics [1, 2]. The rapid development and commercialization of fast MWIR sources such as interband cascade lasers (ICLs) [3] and quantum cascade lasers (QCLs) [4] in recent years has increased the demand for high-speed MWIR PDs with the balanced DC (low dark current and high responsivity) and RF (high 3-dB bandwidth) performance in areas such as free-space communication [5, 6] and frequency comb spectroscopy [7]. Quantum well infrared photodetectors (QWIPs) [8] and quantum cascade detectors (QCDs) [9, 10] are the potential solutions due to their exceptional high-speed performance. However, these detectors have weak absorption and low responsivity due to the relatively low carrier lifetime [11]. Additionally, these detectors often require light coupling structures to overcome the selection rules for inter-subband transitions. Interband cascade photodetectors (ICPDs), which leverage interband transitions, can overcome the inefficient absorption of normal incident light and have demonstrated GHz-range bandwidths [12, 13]. However, the multiple stage architecture of ICPDs can lead to the current mismatch between stages, which degrades device bandwidth [14]. UTC PDs with T2SLs as absorption layer [15-17], are a promising candidate that exhibit fast electron carrier transport. However, previously reported MWIR high-speed T2SL PDs, including the UTC PDs and ICPDs, require a relatively high reverse bias to achieve a 3-dB bandwidth beyond 5 GHz, leading to high dark current.

The motivation of this work is to demonstrate a high-speed MWIR InAs/GaSb T2SL PD with relatively low dark current and high responsivity. This objective was accomplished by fine-designing the thickness and doping of the absorption layer, along with the InAs drift layer with high electron mobility and the additional relaxation layer which smoothens the conduction band discontinuities. As the later part of this work, we employed a cryogenic dewar packaging on our PD to be user-friendly and allow cryogenic operation for an enhanced adaptability of various application scenarios. As an additional benefit, we also introduce the inductive peaking technique during packaging process using bonding wires, which is commonly used in various NIR high-speed PDs to enhance bandwidth [17-19] at no cost of responsivity and dark current. The original on-wafer PD exhibited a 3-dB bandwidth of 3.83 GHz at -5 V under 300 K with a dark current density of 54.05 A/cm^2 and a responsivity of no less than 0.36 A/W. After being packaged in dewar with inductive peaking, the enhanced 3-dB bandwidth increased to 5.57 GHz at -5V under 300 K. Moreover, under cryogenic operating conditions (T=77 K), the device still achieved a 5.29 GHz 3-dB bandwidth even at -1 V with a dark current density of 1.65×10^{-5} A/cm^2 and a responsivity of 0.39 A/W.

II. MATERIAL GROWTH AND FABRICATION

Fig. 1 shows the epitaxial structure of the UTC PD device, which was grown on the InAs substrate using molecular beam epitaxy (MBE). The growth process began with the deposit of a 50 nm unintentionally doped (uid) InAs buffer, followed by a 1000 nm n-doped InAs layer. A 20-period n-doped 9.3 nm InAs/1.05 nm AlSb T2SLs layer was grown together with the n-doped InAs as the n-contact layer.

Zhijian Shen is with the School of Information Science and Technology, ShanghaiTech University, Shanghai 201210, China, with the Shanghai Institute of Microsystem and Information Technology, Chinese Academy of Sciences, Shanghai 200050, China, and also with the University of Chinese Academy of Sciences, Beijing 100049, China (e-mail: shenzhj1@shanghaitech.edu.cn).

Jian Huang, Zhecheng Dai, Luyu Wang, Fengyu Liu, Xinbo Zou and Baile Chen are with the School of Information Science and Technology, ShanghaiTech University, Shanghai 201210, China. Baile Chen is also with the Shanghai Engineering Research Center of Energy Efficient and Custom AI IC, Shanghai 201210, China (e-mail: huangjian@shanghaitech.edu.cn, daizhch@shanghaitech.edu.cn, wangly4@shanghaitech.edu.cn, liufy@shanghaitech.edu.cn, zouxb@shanghaitech.edu.cn, chenbl@shanghaitech.edu.cn).

Jinshan Yao and Hong Lu are with the College of Engineering and Applied Sciences, Nanjing University, Nanjing, Jiangsu Province 210093, China. Hong Lu is also with the Jiangsu Key Laboratory of Artificial Functional Materials, Nanjing University, Nanjing, Jiangsu Province 210093, China (email: yaojinshan@smail.nju.edu.cn, hlu@nju.edu.cn).

Bo Peng and Weimin Liu are with the School of Physical Science and Technology, ShanghaiTech University, Shanghai 201210, China (email: pengbo@shanghaitech.edu.cn, liuwm@shanghaitech.edu.cn).

Next, a 400 nm uid InAs layer was introduced as the drift layer. Then, an 8-stage uid InAs/AlSb multi quantum well (MQW) layer was used as the relaxation layer to smoothen the conduction band discontinuities. After that, to create a quasi-electric field that facilitates electron transport in the absorption layer, three 55-period and one 33-period 2.4 nm InAs/2.1 nm GaSb T2SLs layers were grown with step graded doping. Since a higher p-doping could lead to a higher Auger recombination rate and a lower excess carrier lifetime that causes poorer responsivity, we apply a medium graded doping level of approximately 1×10^{17} cm^{-3}, 5×10^{16} cm^{-3}, 2×10^{16} cm^{-3}, and 1×10^{16} cm^{-3}. Then, a 20-period p-doped 1.8 nm AlSb/4.8 nm GaSb T2SLs electron barrier layer was grown to prevent electrons in the absorption layer from diffusing into the p-contact layer. Finally, a 20 nm thick p-doped InAs was added as the p-contact layer. In contrast to our previously reported InAs/GaSb T2SL MWIR UTC PD in 2020 [15], this structure has a thicker absorption layer to achieve better responsivity, and we use InAs instead of InAs/AlSb as drift layer to enhance the electron transport speed in drift layer.

Following the epitaxial growth, the crystal quality of the sample was assessed through high-resolution x-ray diffraction (HRXRD), as illustrated in Fig. 2. The sample has a dominant peak and three distinct sets of satellite peaks, which correspond to the InAs substrate and three T2SLs layers: the n-contact layer of 9.3 nm InAs/1.05 nm AlSb T2SLs (set A), the graded absorption layer of 2.4 nm InAs/2.1 nm GaSb T2SLs (set B), and the block layer of 1.8 nm AlSb/4.8 nm GaSb T2SLs (set C). The satellite peaks in set A exhibited the highest level of ±4th, while those in sets B and C reached ±2nd and ±1st, respectively. The period thicknesses of these T2SLs can be determined by [20]:

$$d = \frac{\lambda}{2\Delta\theta\cos\theta} \qquad (1)$$

where $\lambda = 0.15406$ nm is the wavelength of the X-ray source, θ is the location of the 0th peak of the corresponding set of satellite peaks and $\Delta\theta$ is the interval between the 0th peak and the 1st or -1st peak. The calculated thicknesses of the T2SL layers are $d_A = 10.25$ nm, $d_B = 4.38$ nm, and $d_C = 6.81$ nm, respectively, which are very close to the designed values.

After the HRXRD scan, the sample was fabricated into devices with circular mesa geometries. The mesa structure was etched by an inductively coupled plasma (ICP) dry etch followed by a citric acid-based solution wet etch. Ti/Pt/Au metals were deposited using e-beam evaporation as both the p-metal and n-metal contacts. The surface of the mesa sidewall was passivated with SU-8 photoresist. For high-speed measurement, the p-and n-contacts of the devices were connected to gold-plated ground-source-ground (GSG) pads with 50 Ω characteristic impedance [13].
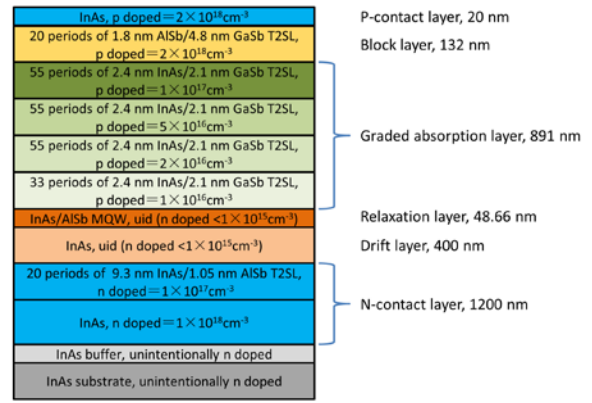

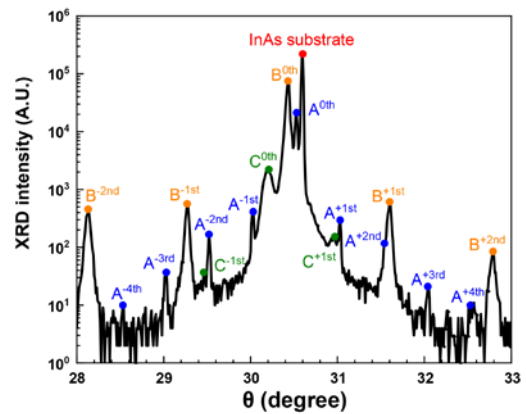Fig. 1. The structure illustration of the high-speed MWIR InAs/GaSb T2SL UTC PD sample.

Fig. 2. The HRXRD scan of the growth sample.

III. Device Characterization

Fig. 3 (a) illustrates the dark current density as a function of bias voltage (J-V) for a 100 μm device across temperatures ranging from 77 K to 300 K. As the temperature increases from 77 K to 300 K, the dark current density increases from 4.44×10^{-6} A/cm^2 to 8.63 A/cm^2 at -0.1 V. Fig. 3(b) shows the dark current density-temperature (J-T) Arrhenius plot at -0.1 V, revealing an activation energy of approximately 220 meV from 300 K to 130 K, and the designed value of bandgap is Eg ≈ 221 meV. Thus, the n-value (n = Eg / Ea) is around 1.005, which is very close to 1, indicating the diffusion mechanism dominates the dark current and a fairly good crystal quality of epi-layers. The moderately large dark current of roughly 100 x Rule 07 at -0.1 V under 300 K is probably mainly due to the p-doping in absorption region, which leads to a higher Auger recombination rate and a lower excess carrier lifetime. For temperatures below 130 K, the tunneling component begins to dominate.

Fig. 4 shows the device capacitance as a function of bias voltage for a 20 μm device at 300 K. Using Eq. (2), we can also calculate and plot the depletion layer thickness:

$$C = \frac{\varepsilon_s\varepsilon_0 S}{d} \qquad (2)$$

where $\varepsilon_s \approx 15.1$ is the relative permittivity, ε_0 is the vacuum permittivity, S is the device area and d is the

thickness of depletion layer. As can be seen from Fig. 4, the drift layer isn't fully depleted until reverse bias reaches -3 V. For higher reverse bias beyond -3 V, in addition to the fully depleted drift layer, a small part at the edge of p-doped absorption layer will be depleted since the thickness of depletion layer becomes larger than 400 nm.
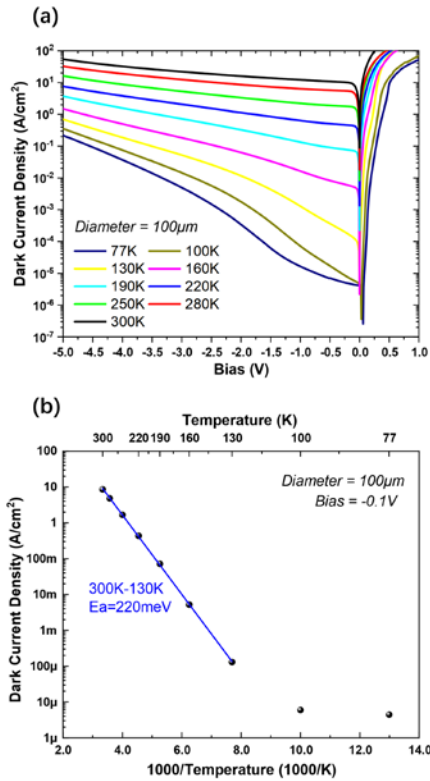

Fig. 3. (a) The J-V curve for a 100 μm device at different temperatures. (b) The Arrhenius plot and linear fit for the dark current density under −0.1V.
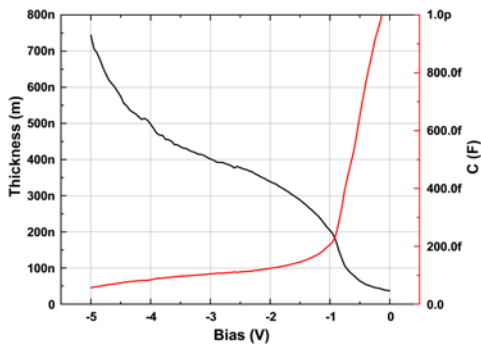

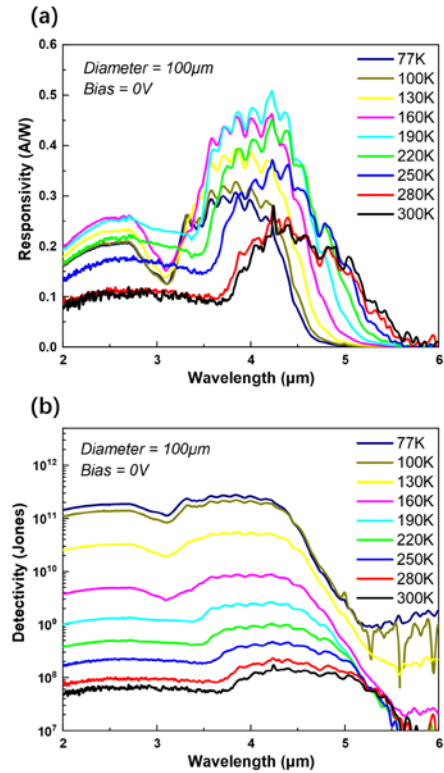Fig. 4. The C-V curve for a 20 μm device at 300K and the corresponding calculated d-V curve.

Fig. 5. (a) The responsivity curve of a 100 μm device under various temperatures at 0 V. (b) The corresponding calculated Johnson-noise and shot-noise limited detectivity.

The responsivity of the device was measured by a Fourier transform infrared (FTIR) spectrometer and calibrated by a blackbody source. Fig. 5 (a) shows the 0 V responsivity of a 100 μm device at various temperatures. As the temperature increases from 77 K to 300 K, the cutoff wavelength redshifts from 5.1 μm to 5.6 μm. From 77 K to 190 K, the responsivity rises with temperature. This is due to the narrowing of the InAs/GaSb T2SL effective bandgap, leading to stronger absorption. However, as the temperature rises over 190 K, the responsivity decreases significantly, which results from the reduced minority carrier lifetime. The peak responsivity at 4.2 μm under 0 V and 300K is approximately 0.24 A/W. This value corresponds to the quantum efficiency of around 7%, which is higher than previously reported high-speed high speed ICIPs [12, 13], QCDs [9, 10] and InAs/GaSb T2SL UTCs [15] with QE less than 3% (0.1A/W). However, there is still room for optimization. To further increase the QE, one way is introducing an absorption-enhancing technique such as metasurface [21, 22] or backside illumination [23] to increase QE at no cost of bandwidth. Fig. 5 (b) displays the calculated Johnson-noise and shot-noise limited detectivity at 0 V under different temperatures, where the peak detectivity was 1.41×10^8 Jones at 300 K and increased to 2.77×10^{11} Jones at 77 K.

To investigate the high-speed performance, a femtosecond pulse laser with a wavelength of 4.5 μm was employed to characterize the devices, similar to the setup in our previous work [16, 17]. Fig. 6 (a) illustrates the pulse response of a 20 μm device under different biases at 300 K. The amplitude of the electrical pulse increased with rising bias, and at −5 V, the pulse response of the device had a full width at half maximum (FWHM) of approximately 50 ps.

Fig. 6 (b) shows the normalized frequency response of the device, with a 3-dB bandwidth of 1.11 GHz at -1 V and 3.83 GHz at -5 V. Table I summarizes the device's performance under various reverse biases.
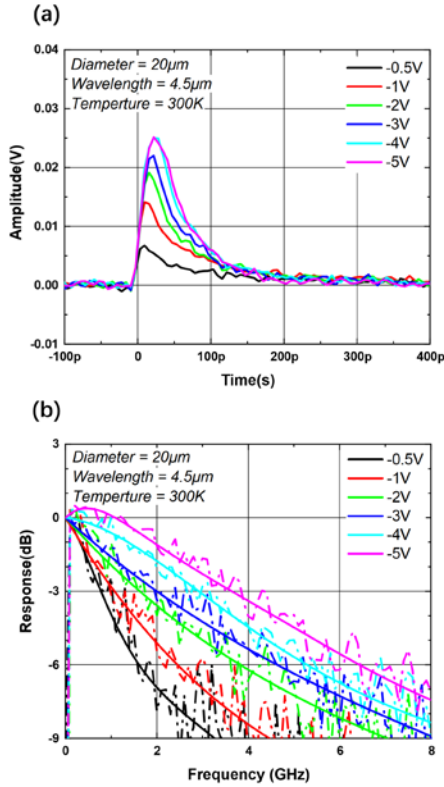

(a)

(b)

Fig. 6. (a) The pulse response of a 20 μm device under different biases at 300 K when irradiated by a 4.5 μm MWIR laser source. (b) The normalized frequency response. The dash-dotted lines are the measured data and the solid lines are polynomial fitting curves, and similarly hereinafter in Fig. 10.

TABLE I
PERFORMANCE SUMMARY OF THE ON-WAFER DEVICE AT 300 K

Bias (V)	Responsivity (A/W)	Dark current density (A/cm²)	3dB bandwidth @4.5 μm (GHz)
0	0.21 @4.5 μm 0.18 @4 μm	/	/
-1	0.23 @4.5 μm 0.19 @4 μm	12.19	1.11
-4	0.36 @4.5 μm 0.27 @4 μm	32.17	3.01
-5	/	54.05	3.83

Additionally, we measured the scattering parameter S11 of a 20 μm device with a vector network analyzer (VNA) to investigate the limiting factor of 3-dB bandwidth. We used an equivalent circuit model similar to Ref [24] to fit the measured S11 curve in Advanced Design System (ADS) software, as shown in Fig. 7 (a). Here, $R_{PD,j1}$ and $C_{PD,j1}$ represent the shunt resistance and junction capacitance of the drift layer, while $R_{PD,j2}$ and $C_{PD,j2}$ model these of the relaxation layer. $R_{PD,s}$ accounts for the contact resistance of the device. We calculated C_{pd-j2} using Eq. (2) and got the calculated value of C_{pd-j2}= 862 fF since d_{pd-j2}=48.66 nm. Fig. 7 (b) and (c) depict the measured and fitted S11 parameters of the device under -1 V and -5 V, with the fitting parameter listed in Table II. Fig. 7 (d) and (e) plot the RC-limited

frequency response $H_{RC-PD}(f)$ under different biases based on the equivalent circuit model, along with the measured frequency response $H_{PD}(f)$ acquired earlier in Fig. 6 (b). The corresponding transit-limited frequency response $H_{transit}(f)$ was estimated based on the Eq. (3) given below:

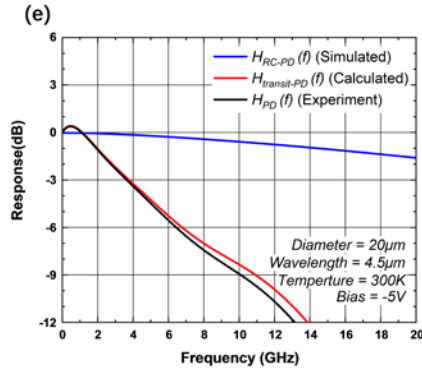$$H_{PD}(f) = H_{transit}(f) * H_{RC-PD}(f) \qquad (3)$$

(a)

(b)   **(c)**

-1V   -5V

(d)
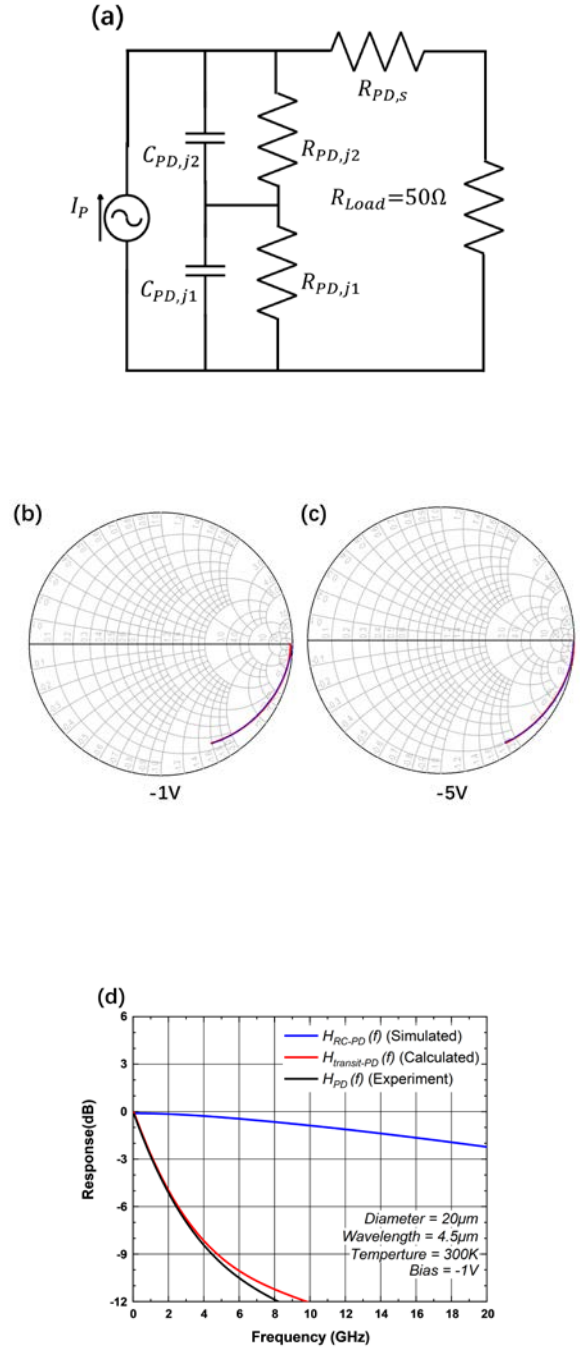
Fig. 7. (a) The PD's equivalent circuit model. (b) (c) The Smith charts presenting the 20 μm device's S11 parameters under -1 V and -5 V. The blue lines are measured values and the red lines are fitting values. (d) (e) The device's separated frequency response under -1 V and -5 V. The blue lines are the RC-limited frequency response, the red lines are the transit-limited frequency response, and the black lines are the total frequency response. The analysis in this set of figures are all based on 300 K condition.

It is worth noting that the RC-limited 3-dB bandwidth of the device is much larger than the transit time limited bandwidth, indicating the bandwidth performance of the PD is primarily limited by the carrier transit time.

TABLE II
FITTING PARAMETERS OF THE ON-WAFER DEVICE

Bias (V)	$R_{PD,j1}$ (Ω)	$C_{PD,j1}$ (fF)	$R_{PD,j2}$ (Ω)	$C_{PD,j2}$ (fF)	$R_{PD,s}$ (Ω)
-1	6420	110.6	20	862	10.7
-5	4486	96.6	20	862	6.2

IV. INDUCTIVE PEAKING AND RE-CHARACTERIZATION

After conducting the on-wafer level device characterization, we optimized device bandwidth performance by modeling the inductive peaking effect using ADS software. To achieve this, we use a new equivalent circuit model, as shown in Fig. 8(a), which consists of three sections. The first section represents the circuit model of the original PD, which is the same to that in Fig. 7 (a). The second section consists of an inductance L_{wire} and a resistance R_{wire} that represent the gold bonding wires. The last part represents the coplanar waveguide (CPW) on printed circuit board (PCB), similar to the model described in Ref [25]. The PD parameters $R_{PD,j1}$, $C_{PD,j1}$, $R_{PD,j2}$, $C_{PD,j2}$ and $R_{PD,s}$ are obtained from

Table II, while The CPW parameters L_{CPW1}, C_{CPW1}, L_{CPW2}, C_{CPW2} and R_{CPW} are determined in advance by fitting the model of the CPW on PCB, as listed in Table III (a). The only undetermined parameters before optimization are L_{wire} and R_{wire}.

The main optimization parameter was L_{wire}, which corresponds to the length of the gold bonding wires l according to the following formula [26]:

$$L_{wire} \approx \frac{\mu_0 l}{2\pi}\left[ln\left(\frac{2l}{a}\right) - 1\right] \quad (4)$$

where $\mu_0 = 4\pi \times 10^{-7}$ H/m is the air medium's permeability and $a = 0.5 mil = 12.7\mu m$ is the radius of the gold bonding wires. The resistance parameter R_{wire} is usually small and only slightly affects the amplitude of the frequency response curve. Using the equivalent circuit model in Fig. 8 (a), we modeled the frequency response with the Eq. (5) below:

$$H_{Dewar}(f) = H_{transit}(f) * H_{RLC-Dewar}(f) \quad (5)$$

where $H_{Dewar}(f)$ is the total frequency response after inductive peaking, $H_{transit}(f)$ is the transit limited frequency response obtained from Fig. 7 (d) (e), and $H_{RLC-Dewar}(f)$ is the resistance-inductance-capacitance (RLC) frequency response. The modeling results suggested that the gold bonding wires should be about 8.8 mm long for 20 μm devices to optimize the inductive peaking bandwidth with the corresponding parameter listed in Table III (b). Fig. 8 (b) and (c) plot the simulated RLC-limited frequency response $H_{RLC-Dewar}(f)$, the transit-limited frequency response $H_{transit}(f)$ obtained from Fig. 7 (d) (e), and the calculated total frequency response $H_{Dewar}(f)$ under -1 V and -5 V.
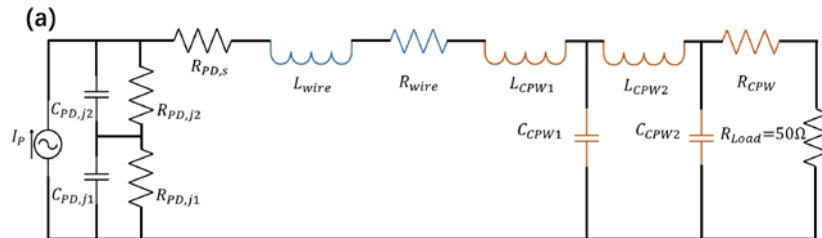
TABLE III (A)
PARAMETERS OF THE CPW ON PCB USED IN SIMULATION

L_{CPW1} (pH)	C_{CPW1} (fF)	L_{CPW2} (pH)	C_{CPW2} (fF)	R_{CPW} (Ω)
2400	500	1300	400	15

TABLE III (B)
PARAMETERS OF THE GOLD BONDING WIRES AFTER OPTIMIZATION

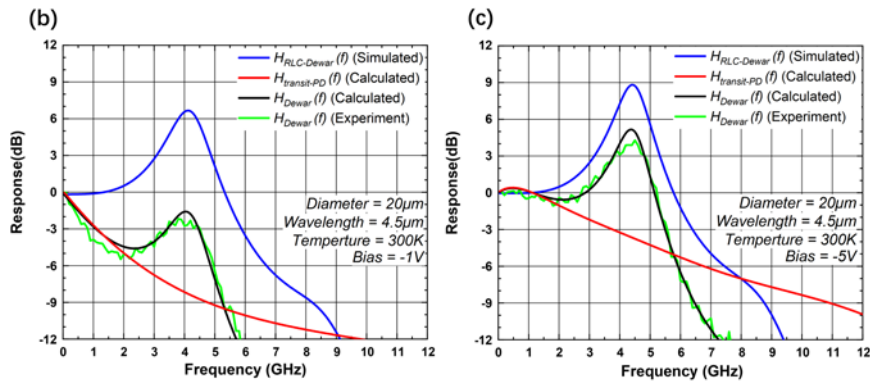| L_{wire} (pH)	R_{wire} (Ω)
1150 (~8.8 mm)	40

(a)

Fig. 8. (a) The equivalent circuit model of the device after inductive peaking. (b) (c) The separated frequency response of a 20 μm device after inductive peaking with optimized parameters under -1 V and -5 V. The blue lines are the RLC-limited frequency response, the red lines are the transit-limited frequency response, and the black lines are the total frequency response. Except for the green lines, all the curves are simulated or calculated values. The green lines give the measured values of the total frequency response. The analysis in this set of figures is all based on 300K condition.
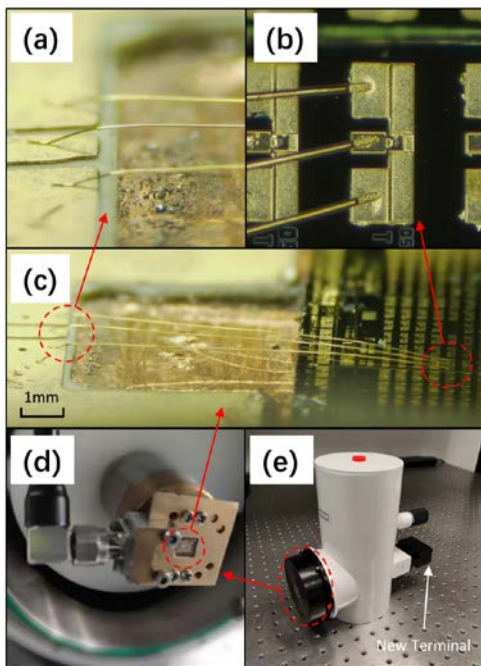

Fig. 9. Photos of the 20 μm PD with inductive peaking packaged in a cryogenic dewar. (a) Gold bonding wires on the CPW side. (b) Gold bonding wires on the GSG pads side. (c) Gold bonding wires between the GSG pads and the ends of the CPW. (d) Internal cable connection. (e) Overall view of the dewar.
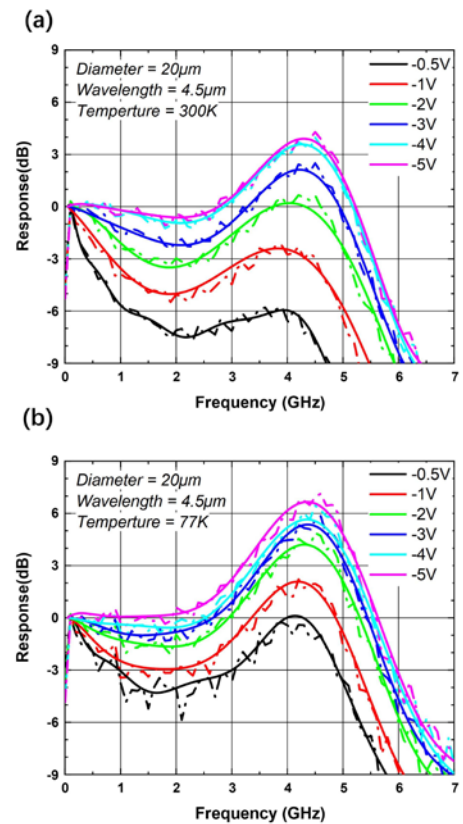

Fig. 10. The normalized frequency response of the inductive-peaked 20 μm packaged device under different biases at (a) 300 K and (b) 77 K when irradiated by a 4.5 μm MWIR laser source.

Afterward, we proceeded to bond the gold wires from the device's GSG pads to the CPW on PCB. The measured wire length, which closely matched to the modeling value, was approximately 9 mm, as shown in Fig. 9 (a) (b) (c). Subsequently, we packaged the entire device in a dewar to enable its operation under cryogenic conditions, as illustrated in Fig. 9 (d) (e). We then measured the frequency response of the 20 μm packaged device, as depicted in Fig. 8 (b) (c), which was consistent with the modeled value. At 300 K, the 3-dB bandwidth of the inductive-peaked PD sample is 0.84 GHz under -1 V bias and increases to 5.57 GHz under -5 V. Meanwhile, at 77 K, the inductive-peaked PD sample achieved a 3-dB bandwidth of 5.29 GHz at -1 V bias and increased to 5.98 GHz at -5 V, as shown in Fig. 10.

A performance summary of the inductive-peaked 20 μm packaged device is provided in Table IV.

TABLE IV (A)
PERFORMANCE SUMMARY OF THE INDUCTIVE-PEAKED DEVICE ENCAPSULATED IN A DEWAR AT 300 K

Bias (V)	Responsivity (A/W)	Dark current density (A/cm^2)	3dB bandwidth @4.5 μm (GHz)
0	0.21 @4.5 μm 0.18 @4 μm	/	/
-1	0.23 @4.5 μm 0.19 @4 μm	12.19	0.84
-4	0.36 @4.5 μm 0.27 @4 μm	32.17	5.53
-5	/	54.05	5.57

TABLE IV (B)
PERFORMANCE SUMMARY OF THE INDUCTIVE-PEAKED DEVICE ENCAPSULATED IN A DEWAR AT 77 K

Bias (V)	Responsivity (A/W)	Dark current density (A/cm^2)	3dB bandwidth @4.5 μm (GHz)
0	0.07 @4.5 μm 0.29 @4 μm	/	/
-1	0.11 @4.5 μm 0.39 @4 μm	1.65×10^{-5}	5.29
-4	0.17 @4.5 μm 0.45 @4 μm	0.037	5.92
-5	0.18 @4.5 μm 0.45 @4 μm	0.22	5.98

V. CONCLUSION

In conclusion, this study has presented a high-speed MWIR InAs/GaSb type-II T2SL UTC PD with balanced DC and RF performance. The original on-wafer PD exhibits a dark current density of 54.05 A/cm^2 and a 4.5 μm of no less than 0.36 A/W, with a 3-dB bandwidth of 3.83 GHz. The inductive-peaked device in dewar packaging shows a dark current density of 1.65×10^{-5} A/cm^2 and a 4 μm responsivity of 0.39 A/W at 77 K, with a 3-dB bandwidth of 5.29 GHz. These promising results could potentially have a significant impact on MWIR high-speed applications.

ACKNOWLEDGMENT

REFERENCES

[1] D. O. Alshahrani, M. Kesaria, E. A. Anyebe, V. Srivastava, and D. L. Huffaker, "Emerging Type‐II Superlattices of InAs/InAsSb and InAs/GaSb for Mid‐Wavelength Infrared Photodetectors," *Advanced Photonics Research,* vol. 3, no. 2, 2021.

[2] D. Jung, S. Bank, M. L. Lee, and D. Wasserman, "Next-generation mid-infrared sources," *Journal of Optics,* vol. 19, no. 12, 2017.

[3] I. Vurgaftman, W. W. Bewley, C. L. Canedy, C. S. Kim, M. Kim, J. Ryan Lindle, C. D. Merritt, J. Abell, and J. R. Meyer, "Mid-IR Type-II Interband Cascade Lasers," *IEEE Journal of Selected Topics in Quantum Electronics,* vol. 17, no. 5, pp. 1435-1444, 2011.

[4] Y. Yao, A. J. Hoffman, and C. F. Gmachl, "Mid-infrared quantum cascade lasers," *Nature Photonics,* vol. 6, no. 7, pp. 432-439, 2012.

[5] C. Liu, S. Zhai, J. Zhang, Y. Zhou, Z. Jia, F. Liu, and Z. Wang, "Free-space communication based on quantum cascade laser," *Journal of Semiconductors,* vol. 36, no. 9, 2015.

[6] A. Soibel, M. W. Wright, W. H. Farr, S. A. Keo, C. J. Hill, R. Q. Yang, and H. C. Liu, "Midinfrared Interband Cascade Laser for Free Space Optical Communication," *IEEE Photonics Technology Letters,* vol. 22, no. 2, pp. 121-123, 2010.

[7] L. A. Sterczewski, J. Westberg, M. Bagheri, C. Frez, I. Vurgaftman, C. L. Canedy, W. W. Bewley, C. D. Merritt, C. S. Kim, M. Kim, J. R. Meyer, and G. Wysocki, "Mid-infrared dual-comb spectroscopy with interband cascade lasers," *Opt Lett,* vol. 44, no. 8, pp. 2113-2116, Apr 15, 2019.

[8] E. Rodriguez, A. Mottaghizadeh, D. Gacemi, D. Palaferri, Z. Asghari, M. Jeannin, A. Vasanelli, A. Bigioli, Y. Todorov, M. Beck, J. Faist, Q. J. Wang, and C. Sirtori, "Room-Temperature, Wide-Band, Quantum Well Infrared Photodetector for Microwave Optical Links at 4.9 μm Wavelength," *ACS Photonics,* vol. 5, no. 9, pp. 3689-3694, 2018.

[9] J. Hillbrand, L. M. Krüger, S. Dal Cin, H. Knötig, J. Heidrich, A. M. Andrews, G. Strasser, U. Keller, and B. Schwarz, "High-speed quantum cascade detector characterized with a mid-infrared femtosecond oscillator," *Optics Express,* vol. 29, no. 4, pp. 5774-5781, 2021.

[10] T. Dougakiuchi, A. Ito, M. Hitaka, K. Fujita, and M. Yamanishi, "Ultimate response time in mid-infrared high-speed low-noise quantum cascade detectors," *Applied Physics Letters,* vol. 118, no. 4, pp. 041101, 2021.

[11] W. Huang, S. M. S. Rassel, L. Li, J. A. Massengale, R. Q. Yang, T. D. Mishima, and M. B. Santos, "A unified figure of merit for interband and intersubband cascade devices," *Infrared Physics & Technology,* vol. 96, pp. 298-302, 2019.

[12] Y. Chen, X. Chai, Z. Xie, Z. Deng, N. Zhang, Y. Zhou, Z. Xu, J. Chen, and B. Chen, "High-Speed Mid-Infrared Interband Cascade Photodetector Based on InAs/GaAsSb Type-II Superlattice," *Journal of Lightwave Technology,* vol. 38, no. 4, pp. 939-945, 2020.

[13] Z. Xie, J. Huang, X. Chai, Z. Deng, Y. Chen, Q. Lu, Z. Xu, J. Chen, Y. Zhou, and B. Chen, "High-speed mid-wave infrared interband cascade photodetector at room temperature," *Optics Express,* vol. 28, no. 24, pp. 36915-36923, 2020.

[14] B. Chen, "Equivalent circuit model of the RF characteristics of multi-stage infrared photodetectors," *Journal of Lightwave Technology,* vol. 40, no. 15, pp. 5224-5230, 2022.

[15] J. Huang, Z. Xie, Y. Chen, J. E. Bowers, and B. Chen, "High Speed Mid-Wave Infrared Uni-Traveling Carrier Photodetector," *IEEE Journal of Quantum Electronics,* vol. 56, no. 4, pp. 1-7, 2020.

[16] J. Huang, Z. Dai, Z. Shen, Z. Wang, Z. Zhou, Z. Wang, B. Peng, W. Liu, and B. Chen, "High-Speed Mid-Wave Infrared InAs/InAsSb Superlattice Uni-Traveling Carrier Photodetectors With Different Absorber Doping," *IEEE Transactions on Electron Devices,* vol. 69, no. 12, pp. 6890-6896, 2022.

[17] J. Huang, Z. Shen, Z. Wang, Z. Zhou, Z. Wang, B. Peng, W. Liu, Y. Chen, and B. Chen, "High-speed Mid-wave Infrared Uni-traveling Carrier Photodetector Based on InAs/InAsSb Type-II Superlattice," *IEEE Electron Device Letters,* vol. 43, no. 5, pp. 745-748, 2022.

[18] G. Chen, Y. Yu, S. Deng, L. Liu, and X. Zhang, "Bandwidth improvement for germanium photodetector using wire bonding technology," *Opt Express,* vol. 23, no. 20, pp. 25700-6, Oct 5, 2015.

[19] A. Novack, M. Gould, Y. Yang, Z. Xuan, M. Streshinsky, Y. Liu, G. Capellini, A. E. Lim, G. Q. Lo, T. Baehr-Jones, and M. Hochberg, "Germanium photodetector with 60 GHz bandwidth using inductive gain peaking," *Opt Express,* vol. 21, no. 23, pp. 28387-93, Nov 18, 2013.

[20] S. A. Speakman, "Estimating crystallite size using XRD," *MIT Center for Materials Science and Engineering,* vol. 2, pp. 14, 2014.

[21] T. Wenger, R. Muller, D. Wilson, S. D. Gunapala, and A. Soibel, "Large metasurface-based optical concentrators for infrared photodetectors," *AIP Advances,* vol. 11, no. 8, 2021.

[22] T. Wenger, R. Muller, C. J. Hill, A. Fisher, D. Z. Ting, D. Wilson, S. D. Gunapala, and A. Soibel, "Infrared nBn detectors monolithically integrated with metasurface-based optical concentrators," *Applied Physics Letters,* vol. 121, no. 18, 2022.

[23] P.-Y. Delaunay, B. M. Nguyen, D. Hofman, and M. Razeghi, "Substrate removal for high quantum efficiency back side illuminated type-II InAs／GaSb photodetectors,*"* *Applied Physics Letters,* vol. 91, no. 23, 2007.

[24] M. Natrella, C. P. Liu, C. Graham, F. van Dijk, H. Liu, C. C. Renaud, and A. J. Seeds, "Accurate equivalent circuit model for millimetre-wave UTC photodiodes," *Opt Express,* vol. 24, no. 5, pp. 4698-4713, Mar 7, 2016.

[25] Y. Han, B. Xiong, C. Sun, Z. Hao, J. Wang, Y. Han, L. Wang, H. Li, J. Yu, and Y. Luo, "Distributed parameter circuit model for wideband photodiodes with inductive coplanar waveguide electrodes," *Chinese Optics Letters,* vol. 18, no. 6, 2020.

[26] C. Wang, J. Zheng, G. Wang, W. Gao, and Q. Hua, "Parasitic Effects Analysis of Bonding Wires Bonding Parameter of Intelligent Power Modules for Three-Phase Motor Control Applications," *Journal of Physics: Conference Series,* vol. 1607, no. 1, 2020.